Schweizerische Eidgenossenschaft
Confédération suisse
Confederazione Svizzera
Confederaziun svizra

Eidgenössisches Departement für
Umwelt, Verkehr, Energie und Kommunikation UVEK

Bundesamt für Energie BFE

Final report 5. Januar 2012

ETA SOLAR CELL

Extremely thin absorber solar cell based on electrodeposited ZnO nanostructures

Auftraggeber:
Bundesamt für Energie BFE
Forschungsprogramm Photovoltaik
CH-3003 Bern
www.bfe.admin.ch
Auftragnehmer:
EMPA-Materials Science & Technology, Laboratory for Mechanics of Materials and Nano-structures.
Feuerwerkerstrasse 39
CH-3602 Thun
www.empa.ch
Autoren:
Jamil Elias, Laetitia Philippe, Johann Michler
Laboratory for Mechanics of Materials and Nanostructures. EMPA – Materials Science and Technology
Jamil.Elias@empa.ch
Laetitia.Philippe@empa.ch
Johann.Michler@empa.ch

BFE-Bereichsleiter: Dr. Stefan Oberholzer
BFE-Programmleiter: Dr. Stefan Nowak
BFE-Vertrags- und Projektnummer: SI/500426 / SI/500426-01

Für den Inhalt und die Schlussfolgerungen ist ausschliesslich der Autor dieses Berichts verantwortlich.

1. Summary

In this project, systematic and fundamental studies on the synthesis of new nanostructured semiconducting materials have been performed by electrochemical deposition approach combined with natural lithography and atomic layer deposition. The effect of nanostructure's dimensions and architectures on the optical engineering through the n-type semiconductors (ZnO) have been studied in order to control the light scattering for application in nanostructured solar cells particularly for extremely thin absorber (ETA). A dramatic improvement of light diffusion has been found by using the present new ZnO architecture, namely urchin-like. A clear correlation between the light scattering engineering and the light absorption has been demonstrated after the deposition of an ultrathin layer of a light absorber (CdSe) on the ZnO nanostructures. In a later stage of the project, control of the CdSe thickness has been assessed in order to obtain an optimal thickness for charge separation and avoiding recombination. This was followed by a full control of the p-type semiconductor (CuSCN) thickness over the core-shell ZnO/CdSe arrays. Finally, ETA solar cells including the optimized thicknesses of light absorber and p-type semiconductor have been fabricated with different ZnO urchin-like dimensions. A perfect correlation between the dimensions, the light diffusion, the light absorption and solar cells efficiency have been obtained. As results, the light diffusion of the urchin-inspired nanowire arrays was varied from 15% to 35%. Homogenous absorption in the wavelength range of 400-800 nm of up to 90% was obtained. First results show ~1.33% solar conversion efficiencies. This will open important rooms of improvement for ZnO urchin-like based nanostructured solar cells in general and particularly for ETA.

2. Abstract

High surface area nanowire based architectures have been identified as important components for future optoelectronic nanodevices, solar cells, wettability coatings, gas sensors, and biofuel cells. Here we report on a novel urchin-inspired nan-owire architecture: its interwoven three-dimensional, high-surface-area nanowire arrangement can be precisely controlled by using a low-cost and scalable synthesis based on a combination of nanosphere lithography, low-temperature atomic layer deposition, and electrodeposition. The performance of single-layer arrays of urchin-inspired ZnO nanowire building blocks competes to that of planar nanowire carpets. We illustrate this capability by fabricating fully-inorganic extremely thin absorber solar cells using CdSe as absorber and CuSCN as hole-collector material. The light diffusion of the urchin-inspired nanowire arrays was varied from 15% to 35%. Homogenous absorption in the wavelength range of 400-800 nm of up to 90% was obtained. Solar conversion efficiencies of ~ 1.33% were achieved.

3. Introduction

According to a recent study on the global power plant market realized by Greenpeace International the installed capacity of solar power grew faster than that of any other power technology. Third generation (TG) nanostructured photovoltaic devices including dye sensitized (photoelectrochemical, quasi-solid, and solid-state) solar cells and their hybrid or fully inorganic variants (extremely thin absorber (ETA) solar cells) appear to have a big economical potential compared to the basic photovoltaic devices (Si solar cells). Additionally, they are promising candidates for achieving the basic criteria for large scale commercialization: they are highly efficient devices that employ low-cost materials and offer the possibility of being fabricated by large-scale and inexpensive (solution processing) techniques. The main difference with respect to conventional first generation (FG) solar cells resides in their photoconversion mechanism [1]. In the traditional silicon photovoltaic devices the absorption of light leads to the direct formation of free electron–hole pairs in the bulk of the material and the direct production of charge carriers.[2] In TG, the presence of organic or inorganic semicon-

ductors implies that the absorption of photons from sunlight produces an exciton, a tightly bound electron–hole pair, which must be split for charge generation.[3] Exciton dissociation takes place at the interface between the constituent semiconductors. Thus, TG encompasses photovoltaic systems largely dependent on interfacial processes. The reliance on the crystallinity of the materials for photovoltaic response indicates that while highly crystalline and chemically pure materials are required for FG solar cells, less pure and therefore less expensive compounds can be applied in TG Solar Cells (e.g. ZnO and TiO_2).[4] Although first generation SCs have the advantage of high efficiency (~ 20%) and long lifetime (25 years), state-of-the-art of TG have improved enormously in the past few years demonstrating efficiencies as high as 11.3% [5] and lifetimes of 10 000 h for Dye-sensitized solar cells (DSC) and about 5–6% efficiency for Organic Solar cells (OSC) [6]. These promising results have encouraged many research groups, as well as industrial partners, to investigate different ways to improve TG Solar Cells performance, especially device efficiency and lifetime. Among different types of TG, ETA Solar Cells appear to be the most promising one because it's completely based on inorganic semiconductor which can avoid the problems of stability at high temperatures under full sun irradiation encountered in DSC and OSC (due to nature of dye and electrolyte in DSC and polymers in OSC).

In the field of PV, scientific interest in nanostructures and especially in nanorods (NRs, also known as nanowires-NWs) materials increased sharply in the last ten years, if the overall outcome of scientific publications is taken as an indicator. A search for NR or NW publications in ISI Web of Knowledge database reveals that the number of publications increased by more than 40 times during the last decade, from 150 publications in 1997 to 6000 publications in 2010. The corresponding increase in research activities is to some extent caused by the fact that a huge variety of materials, literally ranging from A like AlN [7] to Z like ZnO [8], can be synthesized as needle-like, NRs or NWs by using different techniques. This is not only true for NRs fabricated by top-down structuring methods like reactive ion etching, but also and in particular for bottom-up approaches.

In recent years, single-crystal ZnO NW arrays have emerged as promising building blocks for a new generation of devices in different technological domains such as wide range of applications, like short-wavelength lasers,[9] piezoelectric nanogenerators,[10] electroluminescence,[11] and field-emission devices [12] apart from solar cells. This is not only due to the high capabilities of ZnO as a multifunctional material but also due to the particular morphology of the NW arrays. Until now, most of the research on the deposition methods has mainly been focused on vapor-phase techniques.[13] A common characteristic of these kind of techniques is the high temperature. Temperatures of 900-1100 °C are the most frequently used in vapor-liquid-solid processes, while lower temperatures of 400-500 °C are used in free-catalyst and more sophisticated techniques such as metal-organic chemical vapor deposition. Electrochemical deposition of ZnO NW arrays, from the reduction of molecular oxygen in aqueous solutions, is a convenient low-temperature (<100 °C) alternative.[14,15] Aside from the fact that this technique is well-suited for large-scale production processes, electrodeposited ZnO NW arrays have already shown great potentiality in nanostructured solar cells,[16] ultraviolet (UV) electroluminescent hybrid light emitting diodes,[17] and UV nanolasers.[18]

4. Objectives

In this project, the objective was to make a highly innovative contribution by suggesting and exploring a novel concept for thin film solar cells (SC) based on low-cost electrodeposited arrays of ZnO nanostructures (as a n-type semiconductor) bearing the potential for solar cell efficiencies exceeding the 15% limit in a micrometer thin layer due to structural and cell design peculiarities [19]. These peculiarities are: (i) the nanostructures of ZnO are inherently free of extended lattice defects and (ii) the p-n junction in the solar cell for charge separation can be realized radially (in the case of 1D nanostructured ZnO) so, that light absorption and generated carrier diffusion to the p-n junction can be decoupled into orthogonal directions and diffusion distances are short.

Being fully explored and developed, such a nanostructured (including nanowires, nanorods, and complex architectures) based solar cell represents a major break-through in thin film photovoltaic on cheap glass or foil substrates [20]. Thus, the nanostructured photovoltaic concepts are free of the usual thin film problems that hamper good solar cell efficiencies such as low grain size, high defect density and thus limited diffusion lengths and high carrier recombination. It is, however, essential for the industrial solar cell implementation that such a process will not be more expensive than the established pure solid phase crystallization (SPC) of amorphous silicon (a-Si) films on glass that serves as a benchmark. This is why the electrochemical synthesis is the obvious solution to circumvent the use of high cost high vacuum synthesis methods.

An increase in European competitiveness for the field of thin film photovoltaic is targeted by the project and will affect Swiss photovoltaic module manufacturers, equipment manufacturers and the scientific community since the electrochemical deposition has the potential to be cheaper than any other deposition method (see next) and Switzerland benefits from a long tradition in plating industry that could be implemented directly to the PV market once proof of concepts of electrodeposited solar cells has been made.

As described earlier, single crystal ZnO layers and NWs have been already electrochemically synthesized in our previous works and a simple cell concept with all materials issues already solved will be assessed directly. It is now important to increase the efficiency of the solar cell by focusing on different parameters such as:

(a) Dimensions, organization and morphology control of ZnO nanostructures

(b) Controlling the light scattering through the ZnO nanostructures

(c) Controlling the light absorption after depositing an ultra-thin layer of narrow band-gap semiconductors on ZnO.

(d) Correlating the light scattering (ZnO) and the light absorption (ZnO/light absorber).

(e) Correlating (d) with the conversion efficiency after the deposition of a p-type material on the core-shell ZnO/light absorber.

In the following are represented the achievements that have been made during this project based on the above goals.

5. Experimental approach

Since this solar cells concept involves different types of materials, different kind of electrochemical and chemical methods have been employed for the synthesis. The details of the deposition process are shown in this part.

A schematic view of ETA solar cells is presented in Figure 1 in order to illustrate the involvement of each material in the fabrication process.

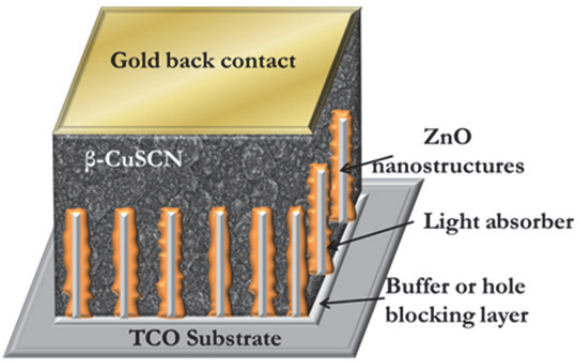


Figure 1 Schematic view of an ETA solar cell based on ZnO nanostructures

5.1 Hole blocking layer

Generally, for this kind of solar cells, a hole-blocking layer barrier is needed in order to avoid short-circuits and contacts between the transparent conductive oxide (TCO) electrode and the p-type semiconductor. Among different methods used in the literature to deposit such thin layers (20-100 nm thickness) we have used the Atomic Layer Deposition (ALD) for the first time. ALD manifests itself as a one of the best technique to deposit highly homogeneous layers on large surface area and onto very complex architectures. [21]

For the deposition process we have used commercial TCO substrates (glass/SnO_2:F, 10 Ω/sq) purchased from Solaronix, Switzerland. The bare TCO were cleaned thoroughly by sonication with soap in water, trichloroethylene (CH_3Cl_3), acetone ($CO(CH_3)_2$) and isopropanol ($CH_3CH(OH)$-CH_3), consecutively, for 15 minutes at 70 °C. After each immersion in each solvent, TCO substrates were rinsed with ultra-pure water and dried in air.

The cleaned TCO substrates have been covered by a thin ZnO nanocrystalline layer by ALD, using diethylzinc (DEZ) and dionized water as zinc oxide (ZnO) precursors. The deposition was performed in 6 steps cycles: a first 0.1 s pulse of DEZ, 20 s of exposure, 45 s of purge (N_2), 1 s pulse of H_2O, 20 s of exposure and 60 s of purge (N_2). Each cycle was lasting 2 min and 26.1 s and deposition of 20 nm of ZnO requires 100 cycles.

5.2 Electrodeposition of ZnO

5.2.1 ZnO nanowire arrays

The electodeposition of ZnO NWs arrays was performed in a three-electrode electrochemical cell using the TCO substrate covered by ZnO buffer layers (see. 5.1) as the cathode, a Pt spiral wire as the counter electrode and a Saturated Calomel Electrode (SCE) as the reference electrode. A schematic view of the set-up and the position of the electrodes are shown in figure 2.

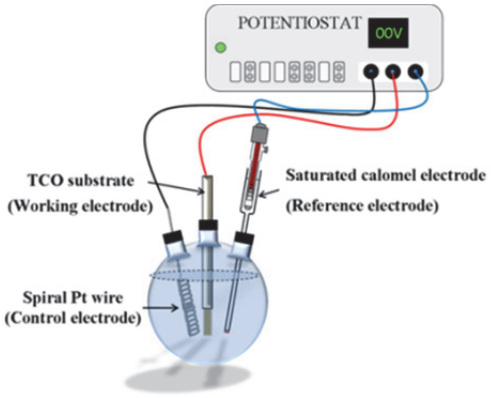


Figure 2 Schematic view of three-electrode electrodeposition system setup used for the electordeposition on ZnO NWs.

We have used the method of oxygen reduction to obtain ZnO NWs. This method consists on an aqueous oxygen saturated solution containing zinc precursor ($ZnCl_2$) and supporting electrolyte (KCl). The temperature was kept constant at 80 °C during the deposition and the potential we applied at -1 V by potentiostat (micro-Autolab). The electrochemical reduction of O_2 occurs by a two (Eq. 1) or a four (Eq. 2) electron process, as a function of the electrolyte and cathode properties. The generation of hydroxide ions induces an increase of the local pH close to the cathode. Zn^{2+} and OH^- ions react together leading to the precipitation of ZnO and deposition on the surface of the cathode (Eq. 3). [22]

$O_2 + 2H_2O + 2e^- \rightarrow 2OH^-$ Eq. 1

$O_2 + 2H_2O + 4e^- \rightarrow OH^-$ Eq. 2

$Zn^{2+} + 2OH^- \rightarrow Zn(OH)_2 \rightarrow ZnO + H_2O$ Eq. 3

The electrolyte was an aqueous solution containing a mixture of $ZnCl_2$ ($5x10^{-5}$-$1x10^{-3}$ M) and KCl (0.05-3.4 M), saturated with bubbling oxygen 10 min before and during the experiment.

The ultrapure water (18 MΩ.cm) was provided by a Millipore setup. Anhydrous $ZnCl_2$ salt (Flucka, purity >98.0 %) was used as the Zn^{2+} precursor. KCl (Flucka, purity >99.5 %) served as a supporting electrolyte. The charge density was varied between 1 and 40 C/cm^2.

5.2.2 Electrodeposition of ZnO urchin-like arrays

A novel approach to fabricate hollow urchin-like ZnO NWs with tailored dimensions has been developed during this project. The method combines the formation of a polystyrene (PS) microsphere colloidal monolayer, an Atomic Layer Deposition of a thin buffer layer of ZnO and the electrodeposition of ZnO nanowires arrays, followed by the elimination of the PS microspheres (which play the role of a template). The deposition process is shown in the schematic view of Figure 3.

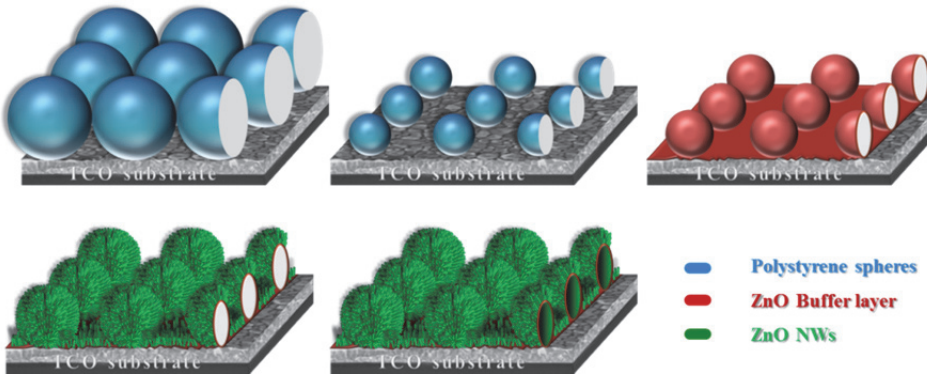


Figure 3 Process steps for the fabrication of ZnO urchin structures: (a) Polystyrene spheres coating on TCO substrate by spin coating; (b) Size reduction of the PS spheres by oxygen plasma etching; (c) Deposition of ZnO buffer layer by Atomic Layer Deposition; (d) Electrodeposition of ZnO nanowires (n-type); (e) PS spheres elimination in toluene.

Firstly, ordered layer of PS microspheres were deposited onto a TCO surface by means of dip coating. More details about this deposition approach can be found elsewhere.[23] The second step consists of reducing the size of the PS spheres under oxygen plasma treatment for 10 minutes by cycle. The size of the PS sphere can be very precisely controlled by choosing an appropriate cycle number. It is important to note that the oxygen plasma treatment leads to a uniform reduction of the PS by maintaining their initial spherical shape. A uniform thin layer of about 20 nm of ZnO is deposited on the ensemble of TCO substrate and the treated PS ordered spheres (see procedure in 5.2.1). Indeed, this thin layer plays in the same time three important roles for the fabrication process. The first one is to fix the PS spheres to the TCO substrates that will be immersed in a further step in an aqueous solution for electrodeposition. This will circumvent a heat treatment at 100 °C after the dip-coating process. The second role of the ALD layer is to render the PS surface electrically active for the use as a conductive electrode for the electrodeposition of ZnO nanowires and the generation of the urchin-like structures. Additionally, for the application of the electrodeposited urchin-like structures in ETA solar cell device, the ZnO ALD deposit plays the role of a buffer layer barrier that can avoid short-circuits (shunts) and contacts between the TCO electrode and the p-type or the hole collector.[24] Contrarily to the traditional use of the polystyrene lithography as nonconductive masks for the deposition in between, here the template will be used as a 3-D electrode (instead of 2-D for planar substrate) and the deposition will take place in the same time on the electrode and the conductive spheres. Once realized, the $TCO/PS/ZnO_{ALD}$ is used as a cathode in a three-electrode electrochemical cell for the electrodeposition of ZnO from the molecular oxygen electroreduction method (see the procedure in 5.2.1).[25]

5.2 Electrodeposition of CdSe

CdSe was deposited electrochemically from an aqueous alkaline selenosulfate solution at room temperature (0.05 M cadmium acetate, 0.1 M nitrilotriacetic acid trisodium salt and 0.005 M selenosulfate, with excess sulphite). The pH of the solution was adjusted by acetic acid to~8-9. CdSe was deposited galvanostatically (J= -3 mA/cm^2) in a two-electrode electrochemical cell with the TCO/ZnObuffer/ZnO$_{NWs}$ samples as cathode and a spiral wire of Pt as a counter electrode. CdSe electrodeposition is based on the reduction of selenosulfate ions (Eq. 4) and the further chemical reaction between Se^{2+} and Cd^{2+} ions (Eq. 5) [26]

$$SeSO_3^{2-} + 2e^- \rightarrow Se^{2-} + SO_3^{2-} \quad \text{Eq. 4}$$

$$Se^{2-} + Cd^{2+} \rightarrow CdSe \quad \text{Eq. 5}$$

The different thicknesses of deposited CdSe on the ZnO nanostructures can be obtained by controlling precisely the charge density (from 0.25 to 0.65 C/cm^2) based on the estimated surface area of the ZnO nanostructures. The deposited CdSe samples were then annealed in air at 350 °C for 1 hour.

5.3 Solution casting of CuSCN

The CuSCN layer is deposited from a saturated solution of CuSCN (~5.75×10^{-2} M, Aldrich, purity ~ 99%) in n-propyl sulfide. The TCO/ZnO$_{Buffer}$/ZnO$_{NWs}$/CdSe samples were preheated at 100 °C on a hot plate. After heating, the CuSCN saturated solution was infiltrated through the core-shell ZnO urchin-CdSe by using a micropipette set to automated bench. A schematic view of the setup is shown in Figure 4. The mechanical arm sweeps the entire surface of the sample uniformly and is controlled by a computer program. The speed is adjusted so that the droplet traverses the surface of the sample and has time to infiltrate slowly. The thickness of CuSCN over the top of NWs was controlled by the volume of CuSCN solution added. A complete filling of the structure is required to obtain a compact layer with a flat surface and to present the best electrical contact.

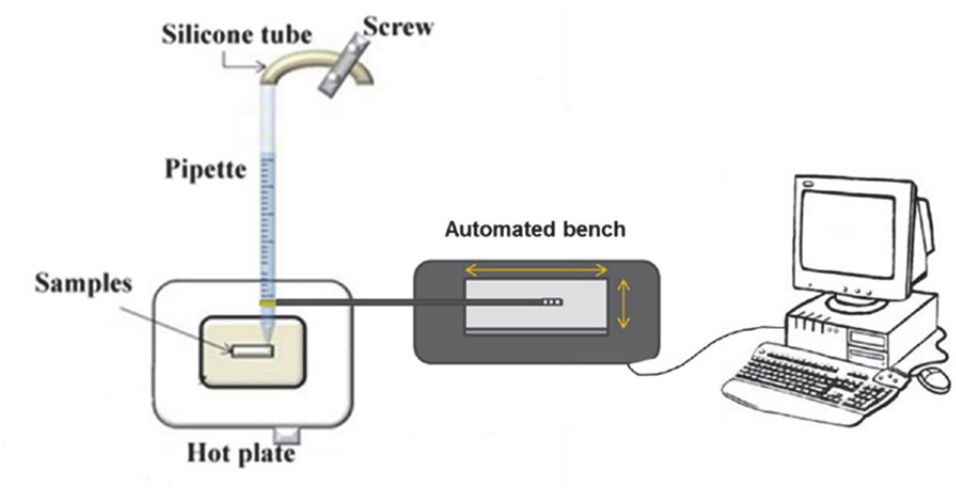


Figure 4 Schematic view of experimental setup for the deposition of CuSCN.

The amount of solution used in the CuSCN deposition process varied between 0.10 and 0.25 ml/cm^2 depending on the needed thickness over the ZnO nanostructured arrays. The volume corresponding to the CuSCN thickness was calculated by using the following equation:

$V_{CuSCN} = 0.0637 \times (L_{NW} + Th_{CuSCN})$

Where V_{CuSCN} is the volume of the CuSCN solution in mL.cm^{-2}, L_{NW} is the length of NWs in µm and Th_{CuSCN} is the thickness of CuSCN from over the urchin structures in µm.

5.4 Sputtering of gold back contacts

To complete the fabrication of ETA-solar cells and provide the electrical contact between the cell and the TCO, 100 nm thin layer of gold was deposited onto the $TCO/ZnO_{buffer}/ZnO_{NWs}$/CdSe solar cells by using plasma sputtering machine (Balzers Union SCD 040). 10 min of sputtering is required to obtain about 100 nm of thickness.

6. Results and discussions

6.1 Controlled synthesis of ZnO

The light scattering of the n-type materials is a very important parameter in order to enhance the optical absorption after adding the ultrathin light absorber layer for the fabrication of the ETA solar cell device. For controlling the light scattering we have studied the variation of dimensions and architectures of ZnO nanostructures by changing the electrochemical parameters and adding different steps to the process. In this part, we show the different studies made for controlling these parameters.

6.1.1 Control of the PS interspace

In order to play on the interspace between the PS spheres, the latter have been etched by oxygen plasma treatment. Cycles of 10 minutes of treatment have been applied and the influence on the size and the surface of the PS has been investigated. SEM images of the PS spheres at different O plasma cycles (i.e. time) are shown in Figure 5.

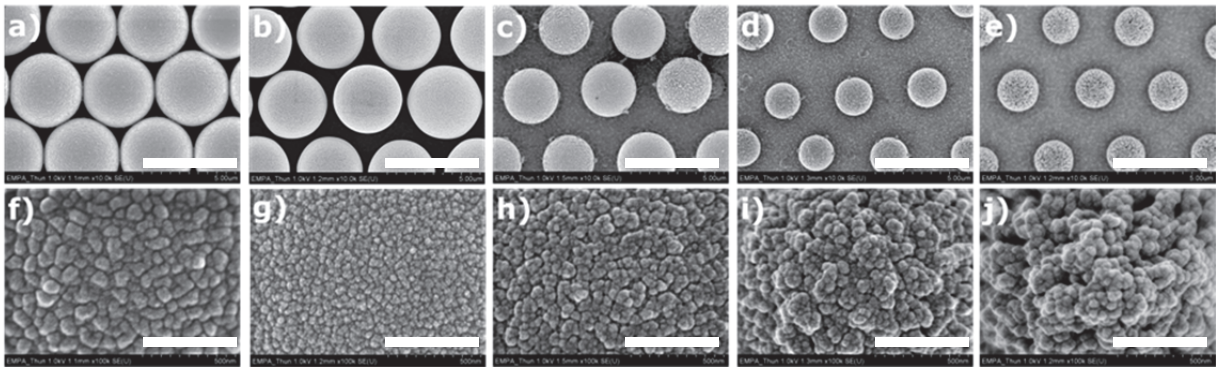


Figure 5 SEM images of PS spheres at different O plasma times: a) 0 min; b) 10 min; c) 20 min; d) 30 min: e) 50 min. f), g), h), i) and j) are the high magnifications of a), b), c), d) and e) respectively. The bar scale in a-f) is 5 µm and the one in f-j) is 500 nm.

The variation of the PS spheres diameter has been estimated from the SEM images of Figures 5a-e and the results are summarized in the graph of the Figure 6.

From the graph of Figure 6, we can clearly see a brutal drop of the PS spheres size in the first 30 min of oxygen plasma treatment as the diameter is reduced from 4 to 2.06 µm (for 0 and 30 min, respectively). After 30 min, the size decreases slowly. On the other hand, the plasma etching affects the PS surface and the surface roughness of PS is clearly increased for long treatment times. High magnifications images of figure 5 (f-j) show that the roughness of the PS spheres is reduced (as the grain size decreased) during the first 10 min of oxygen plasma treatment. In a second time (for O plasma time > 10 min) the roughness increases again with the plasma exposure time.

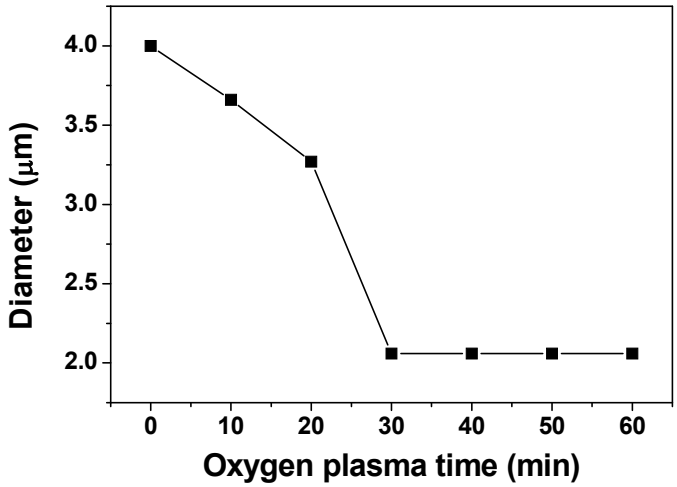


Figure 6 Evolution of the diameter of PS spheres as a function of the O plasma time.

Afterwards, ZnO NWs electrodeposition has been carried out on the different PS arrays of Figure 5, after being coated with 20 nm of ZnO by ALD. The conditions have been fixed to: $[ZnCl_2] = 5.10^{-4}$ M, [KCl] = 0.1 M and the applied charge density was Q = 10 C.cm^{-2}.

The SEM images of the electrodeposited ZnO NWs arrays are shown in Figure 7. We can clearly see an evolution of the nanowires density. As the surface area is reduced with the reduction of the PS spheres; the NWs density logically decreases.

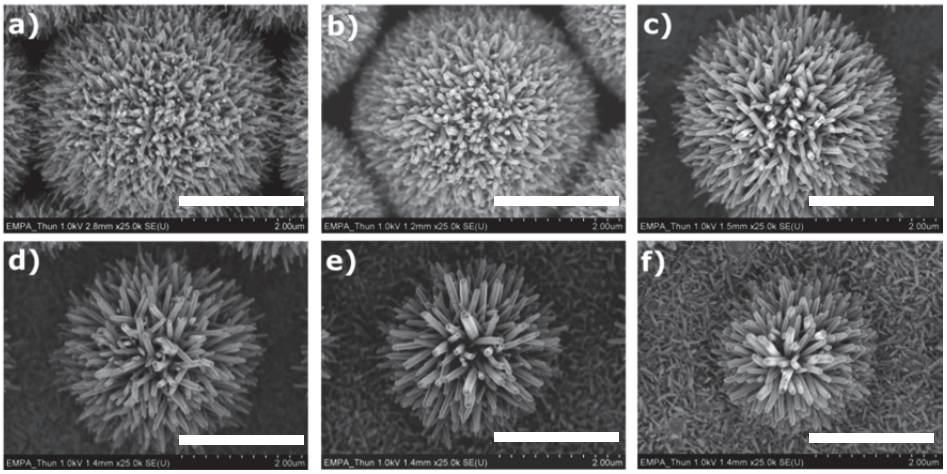


Figure 7 SEM top view images of NWs arrays Urchin-like structure obtained at a) 0 min, b) 10 min, c) 20 min, d) 30 min, e) 40 min, f) 50 min O plasma treatment. The scale bar in all SEM pictures is 2 µm.

An increase of the NWs' diameter can be observed when the size of PS decreases confirming the evolution of surface roughness shown in Figure 5. These results suggest that the roughness of the PS surface plays a role in the NWs growth stage and that the surface roughness can control the NWs dimensions, especially the diameter, during their growth.

In order to illustrate the role of the surface roughness on the NWs growth, deposits obtained with the same O plasma treatment time (equal PS sizes) but presenting different roughness will be shown in the next part.

6.1.2 ALD buffer layer thickness variation

In this part we show the role of the ZnO_{ALD} buffer layer. Different thicknesses of ZnO have been deposited by ALD on similar TCO/PS substrates (O Plasma time = 20 min). High magnification SEM images taken on the PS surfaces are shown in Figure 8.

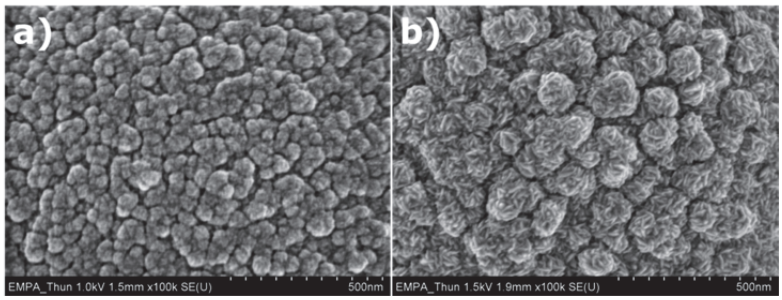


Figure 8 SEM micrographs of TCO/PS/ZnO_{ALD} samples with a) 20 nm, b) 40 nm thickness of ZnO_{ALD} buffer layer.

By increasing the ZnO_{ALD} buffer layer thickness from 20 nm to 40 nm, a noticeable increase in the grain size occurs from ~35-55 nm to ~95-115 nm (determined by the SEM images of Figure 7), respectively. For the moment, the growth mechanisms of these thin layers as well as the evolution of their grain sizes are not yet clear. In order to see the effect of this parameter on the growth of ZnO, deposition of NWs arrays have been carried out on both layers using the same electrodeposition conditions (O plasma 20 min, $[ZnCl_2] = 5.10^{-4}$ M, [KCl] = 0.1 M and Q = 40 $C.cm^{-2}$). The SEM images of the obtained structures are shown in Figure 9.

The dimensions of the obtained NWs arrays after applying a constant charge density of 40 $C.cm^{-2}$ on both layers are clearly different. ZnO_{NWS} deposited on smaller ZnO_{ALD} grain size (~35-55 nm) leads to longer but thinner NWs (length: 1.05 / 0.8 µm; diameter: 180 / 300 nm; for ZnO_{ALD} = 20 / 40 nm, respectively).

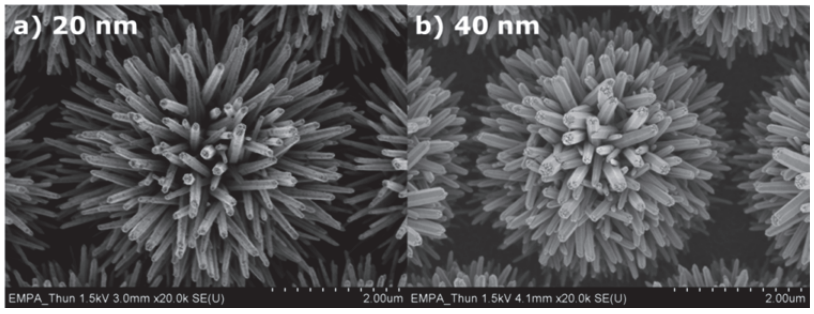


Figure 9 SEM images of NWs arrays Urchin-like structure obtained with different ZnO_{ALD} thickness: a) 20 nm, b) 40 nm.

Therefore, the grain size of the ZnO_{ALD} layer deposit has a major role on the NWs growth. The results of this study demonstrate a change in the growth mechanism when changing the ZnO_{ALD} grain size. The origin of these different growth regimes is most probably due to the nucleation step where the nucleus size can determine the size of crystal obtained in the first growth stage. Therefore, the NW's dimensions at these electrodeposition conditions ($[ZnCl_2] = 5.10^{-4}$ M, [KCl] = 0.1 M) will follow the grain size of the nanograins in the first growth stage.

6.1.3 Charge density effect

In this study, the oxygen plasma time was fixed to 20 min, ZnO_{ALD} thickness to 20 nm, $[ZnCl_2] = 5.10^{-4}$ M and [KCl] = 0.1 M. The charge density was varied in the range from 5 to 40 $C.cm^{-2}$. The top view SEM images of the obtained deposits are shown in Figure 10.

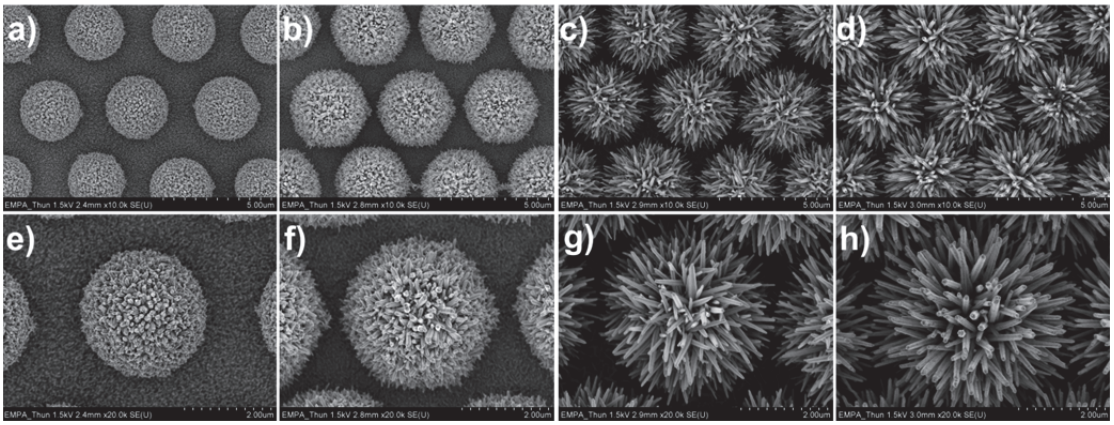


Figure 10 SEM top view images of ZnO ordered urchin-like arrays obtained at different charge densities: a) 5 C/cm^2, b) 10 C/cm^2, c) 30 C/cm^2 and d) 40 C/cm^2. e), f), g) and h) are the high magnifications of a), b), c) and d) respectively.

From Figure 10, a statistical study has been performed in order to estimate the evolution of NWs dimensions as a function of charge density. The obtained values are summarized in the graph of Figure 11.

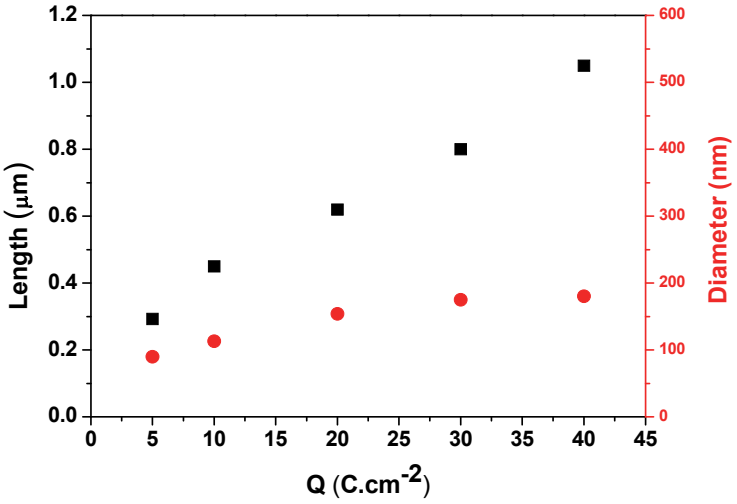


Figure 11 Evolution of the ZnO NWs dimensions (diameters in circles and lengths in squares) as a function of the applied charge density.

From the graph of Figure 11 we can clearly see that the evolution of both dimensions is different. The length evolution (from 290 nm to 1.05 µm) is almost two times faster than the one of diameter (from 90 nm to 180 nm). It is important to note that after passing a charge density of 20 C.cm^{-2}, the increase in diameter is slow and seems to tend to a constant value. Indeed, the diameter increases from 158 to 180 nm when the length almost doubled (from 0.62 to 1.05 µm) for charge densities of 20 and 40 C.cm^{-2}, respectively. Therefore, the increase in diameter after 20 C.cm^{-2} can be considered as insignificant comparing to the length evolution.

These results confirm our previous work [27] showing that under these deposition conditions, the growth along c-axis of the NW is preferentially due to the easier access of Zn^{2+} to the top of the nanowires, resulting in a faster growth orthogonally to this direction.

The variations of the NWs density and the Roughness Factor with the charge density have been estimated and listed in the graphs of Figure 12.

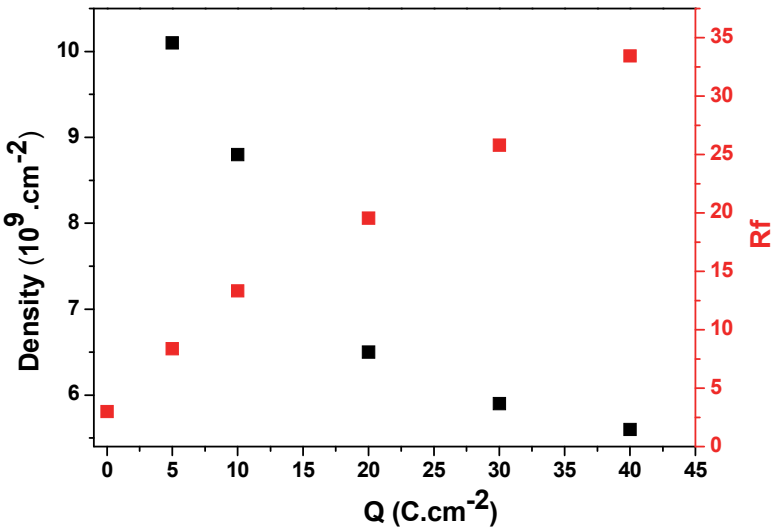


Figure 12 a) Evolution of the density of nanowires arrays and as a function of the charge density (black dots); b) Evolution of the Roughness Factor as a function of the charge density (red circles)

As we mentioned before, the NWs with the easier access for Zn^{2+} ions will grow faster. Therefore, the favored-orientation NWs are longer and hindering (or slowing) the growth of the smaller ones in the lower part. As a result, the NWs density decreases with the increase of charge density (Figure 12).

6.1.4 Role of the zinc precursor concentration

In this part of the project, we have investigated the role of the zinc precursor concentration ([$ZnCl_2$]) on the NWs dimension variation within the urchin like structure. Oxygen plasma time was fixed to 20 min, ZnO_{ALD} thickness deposited was 20 nm, [KCl] = 0.1 M and the applied charge density was kept constant, Q = 10 C.cm^{-2}.

The concentration of $ZnCl_2$ was varied in the range from 5.10^{-5} to 10^{-3} M. For concentrations lower than 5.10^{-5} M, no deposition can be obtained due to the lack of Zn^{2+} ions in the solution. [25] On the other hand, by increasing the concentration to more than 10^{-3} M, $Zn(OH)_2$ will be mainly obtained. [25]

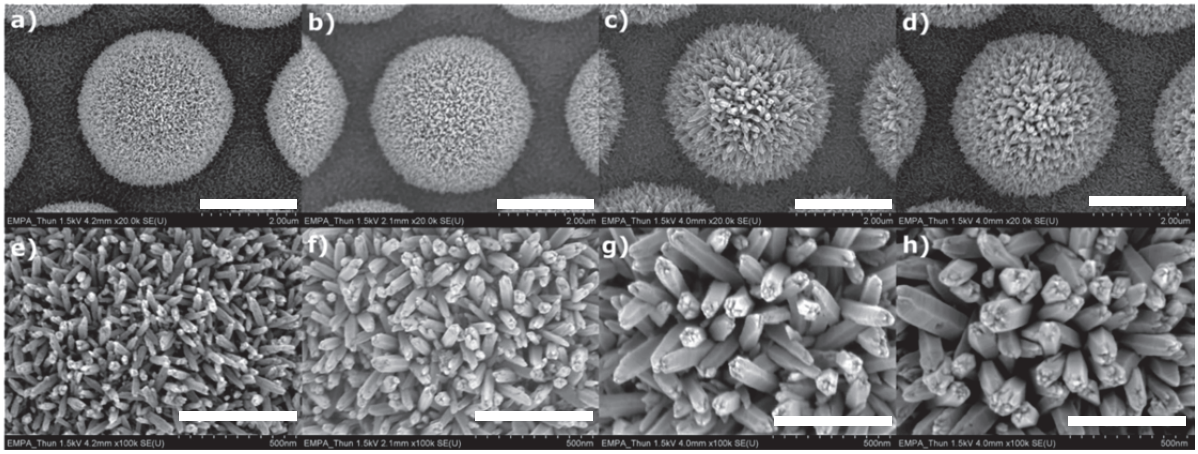


Figure 13 SEM images of ZnO order urchin-like arrays at different concentrations of $ZnCl_2$: a) 5.10^{-5} M; b) 10^{-4} M; c) 5.10^{-4} M; d) 10^{-3} M. e), f), g) and h) are the high magnifications of a), b), c) and d) respectively. The scale bars in a-d) are 2 µm and the ones in e-h) are 500 nm.

Low magnification SEM images in Figures 13a-d indicate that the interspace between the urchin building blocks is almost constant. This also means that, under these conditions, the

NWs length was kept constant. In contrast, closer magnification images in Figures 13 e)-h) show an important evolution of the NWs diameter. A statistical study has been performed and the estimated values of NWs dimensions are summarized in the graph of Figure 14. As can be seen, the length evolution is much less significant than the diameter growth: diameter increases by 4 times while the length rises only by 1.5 times when the [$ZnCl_2$] increases from 5.10^{-5} to 10^{-3} M. Contrarily, the NWs diameter increase about 140% when the concentration of $ZnCl_2$ was increased from 5.10^{-5} to 10^{-3} M.

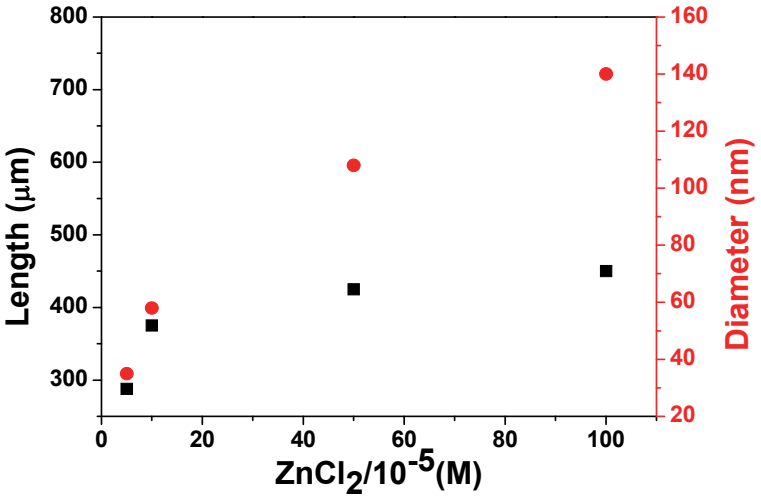


Figure 14 Evolution of the NWs dimensions as a function of the concentration $ZnCl_2$

6.1.5 Role of the supporting electrolyte

In this section we fixed the oxygen plasma time to 20 min, ZnO_{ALD} thickness to 20 nm, [$ZnCl_2$] = 5.10^{-4} M and the charge density was Q = 5 C.cm^{-2}. The role of the supporting electrolyte has been investigated by varying the concentration of [KCl] from 0.1 M to 3 M. The evolution of the mean values of diameter and length of the nanowires shown in the SEM images of Figure 15 are summarized in Figure 16 as a function of [KCl].

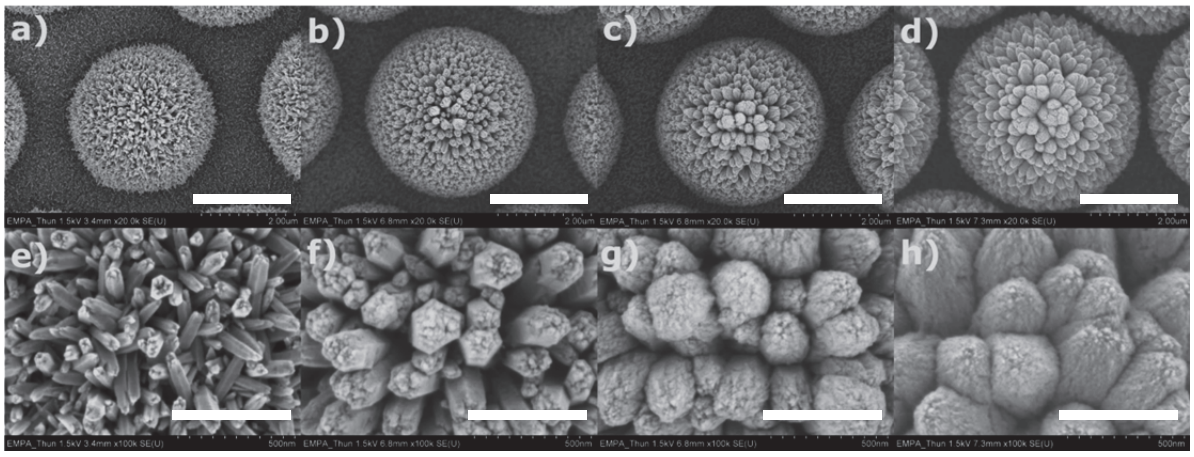


Figure 15 SEM images of ZnO order urchin-like arrays at different concentrations in KCl: a) 0.1 M; b) 1 M; c) 2 M; d) 3 M. e), f), g) and h) are the high magnifications of a), b), c) and d) respectively. The scale bars in a-d) are 2 µm and the ones in e-h) are 500 nm.

At relatively high concentration (>1 M), preferential adsorption of chloride ions on the (0001) ZnO surface (that means the top of the NWs) favors the stabilization of the (0001) face. The adsorption of Cl^- ions on the top of the NWs can slow-down the NWs growth along the *c-axis* and also hinder the electroreduction of O_2 to OH^-. Instead of directly react on top of the NWs, Zn^{2+} ions can diffuse between them and react with OH^- ions that had been electrogenerated

on the lateral faces. This leads to a significant increase of the NWs diameter during the growth. However, the growth remains always faster along the c-axis due to the internal structure of ZnO.

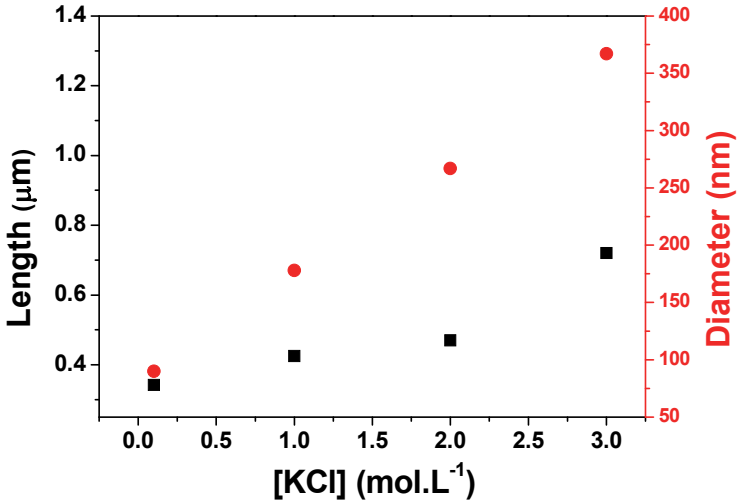


Figure 16 Evolution of the NWs dimensions as a function of the concentration of the supporting electrolyte [KCl].

High diameter's sizes compared to the relative short length of the NWs confer to the Urchin-like structures different morphologies. Indeed for low concentrations of KCl (i.e. 0.1 and 1 M), the nanowires are still separated from each other and distinct NWs arrays are obtained. But for higher concentration (> 2 M) the NWs start to bond with each other, resulting in the coalescence of nanorods and the formation of a compact layer of ZnO.

6.1.6 Conclusions

Different systematic studies have been carried out in this part of the project. The drawn conclusions from the control of the nanostructure dimensions as a function of the different parameters of the process are summarized below:

- The **interspace** between the Urchins can be precisely controlled by controlling the **PS sphere sizes**
- The increase in **charge density** at low supporting electrolyte concentration leads to a preferential growth along the c-axis of the NWs and results in the control of the **length** and the **density of NWs.**
- The concentration of zinc precursor plays an essentially role on the diameter variation.
- The **concentration of the supporting electrolyte** affects both the **length** and the **diameter** of the NWs and plays an important role on the global **architecture** of the Urchin-like structures.

The aim of these studies was to control the dimensions of the ZnO NWs arrays and the morphology of the global structure. The obtained results enable for the first time a **precise control of the diameter and the length of the NWs as well as the interspace and the architecture of the Urchin-like structures**.

6.2 Light scattering of ZnO urchin-like structures

By combining O-plasma treatment, ALD, and electrodeposition, the urchin like ZnO building blocks can be engineered in numerous designs and in a very precise manner. In order to study the geometry influence of the ZnO building-blocks on the light scattering, the spectral

dependence of the optical reflectance (R) of the samples obtained in the previous part of the project (6.1) has been measured and the results are summarized in figure 17. For all analyzed samples, the spectra showed UV absorbance edges close to 375 nm (Eg~3.3 eV), which corresponds to the band-gap energy of bulk ZnO.[28] The first set of measurements concerns the variation of interspace between the urchin-like building blocks (Figure 17a). By increasing the interspace, the maximum of the total reflectance (at λ~400 nm) decreased along with a decrease of the reflectance over the whole wavelength range (from 28% to 17% for interspaces from 0 to 1.5 µm, respectively) whereas only a marginal spectral shift was detected (dotted line, figure 17a). A similar behavior with more pronounced variation has been observed with an increasing NW length while the sphere interspace (3.3 µm) and the ZnO NW diameters (~100 nm) were kept constant (Figure 17b). The total reflectance increased from ~ 15% to 34% (at λ~400 nm) when the NW length increased from 0.3 to 1 µm.

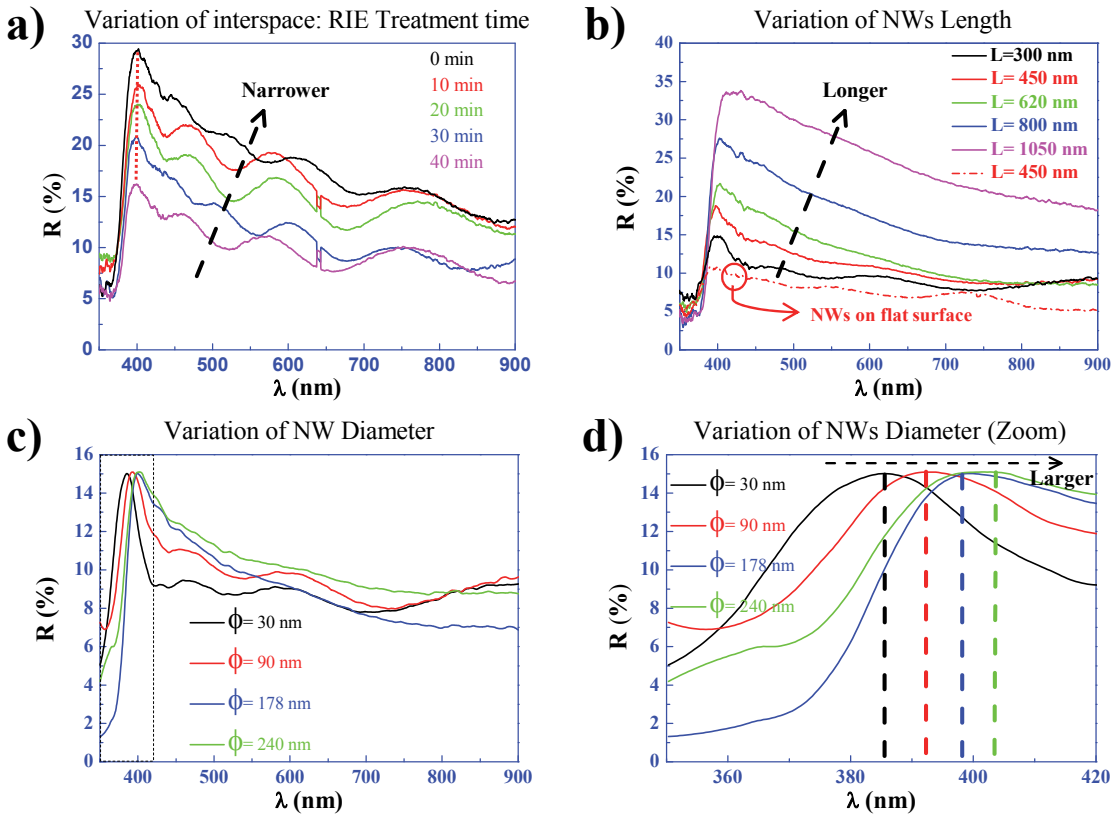


Figure 17 Optical reflectance of the samples obtained in 6.1: a) Variation of interspacing between the urchin-like structures; b) Increasing NW length by keeping constant the sphere interspace (3.3 µm) and the ZnO NW diameters (~100 nm); c) Varying NW diameters and keeping constant the NW lengths (~300 nm) and the sphere interspace (3.3 µm); d) Zoom into the region of UV absorbance edges of Figure 4c.

In order to reflect the importance of the three-dimensional architecture based on urchin-like building-blocks, a ZnO NW carpet was electrodeposited onto a flat FTO substrate that had been covered by a 20 nm thin ALD layer of ZnO. The reflectance of this planar carpet architecture was measured (dashed curve, figure 17b) and compared to the corresponding urchin architecture having the same NWs' dimensions (Figure 17b; diameter~100 nm, length~450 nm). An increase of about 50% of the reflectance was observed throughout the entire visible range. For constant NW lengths (~300 nm) and sphere interspace (3.3 µm), the variation of the NW diameter had no effect on the maximum reflectance value (Figure 17c), however a redshift with increasing diameter was observed (dashed lines, Figure 17d). According to Mie theory [29] the size, the shape, and the distance between the irradiated particles are the main parameters that cover the multiple scattering of the incident light. Due to the complexity

of the 3D urchin-like architecture, the reflectance spectra (Figure 17) can be, for instance, interpreted qualitatively by considering NWs as scattering centers. Regardless of the NWs size, the increase of the interspace between the urchin-like structures decreases progressively the multiple scattering (Figure 17a). This tendency can be explained by the decrease of the size of the urchin-like structures and the larger interspace between them. In other words, when the size of the urchin-like structures decreases less light is trapped by a single structure. Additionally, the target of the reflected light from one structure to another increases with increasing interspace, which leads to a loss of scattered light, and, therefore to a reduction of the total reflectivity of the urchin-like substrates (Figure 17a). Same tendency, but more pronounced, has been found in the case of constant NW diameter and interspace with an increased NW length (Figure 17b). A recent experimental study concerning the effect of ZnO NW size on the light scattering showed that the length of vertical NWs in carpet architecture increases the reflectivity only for a certain wavelength range (400-600 nm). In our urchin-like architecture, the increase of the total reflectivity is found to cover a large wavelength range 400-800 nm. This is most probably due to the fact that NWs are exposed to the incident light from all the directions (i.e. angles) in urchin-like building blocks thus enhancing even more the light scattering. While the increase in the NWs length enhances the maximum of the total reflectivity at fixed wavelength (400 nm), the increase in the diameter size results in a redshift of the whole spectrum (Figures 17c and 17d). We relate this shift to the scattering of the long wavelength visible radiation due to the augmentation of the size of the scattering center when the NWs diameter increases.[27]

6.3 Optimization of different layer thicknesses

The optimization of the absorber (CdSe) and the p-type semiconductor (CuSCN) thicknesses are necessary for having ideal charge separation and transport through and within the different interfaces (ZnO/CdSe and CdSe/CuSCN). It has been shown that the deposited CuSCN thickness over the top of the nanowires arrays is an important factor regarding the efficiency of the complete solar cell. [30] Similarly a compromise between the high photon absorption and the low e^--h^+ pair separation and recombination requires an ideal thickness for the absorber.

In this part of the project, dimensions and architectures of ZnO urchin structures were kept constant. The electrodeposition of ZnO was fixed under these conditions: O plasma time = 20 min, ZnO_{ALD} = 20 nm, [$ZnCl_2$] = 5.10^{-4} M, [KCl] = 0.1 M, Q = 10 C.cm^{-2}. The estimation of the NWs' dimensions confirms the reproducibility of the method (L~450 nm and Φ ~110 nm).

6.3.1 Optimization of the thickness of CdSe

CdSe was electrochemically deposited on similar urchin's dimensions of $TCO/ZnO_{ALD}/ZnO_{NWs}$ electrodes and its thickness has been controlled by controlling the charge density between 0.05 and 0.4 C.cm^{-2}. SEM images of the ZnO urchin arrays coated with thin layers of CdSe at different charge densities are shown in Figure 18. It is important to note that exceeding a charge density of 0.25 C.cm^{-2} (Figure 18d) the distance between the NWs starts to be completely filled and tends to form a compact layer (Figure 18f).

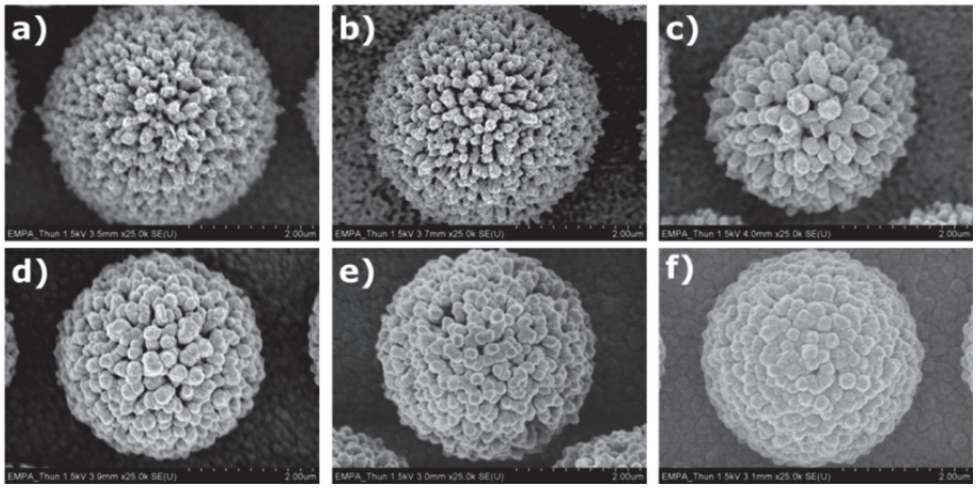


Figure 18 SEM images of TCO/ZnO_{ALD}/ZnO_{NWs}/CdSe covered at different charge densities: a) 0.05 C.cm^{-2}, b) 0.1 C.cm^{-2}, c) 0.15 C.cm^{-2}, d) 0.20 C.cm^{-2}, e) 0.25 C.cm^{-2}, f) 0.4C.cm^{-2}.

A statistical estimation of the electrodeposited CdSe thickness as a function of the charge density has been carried out and the obtained values are shown in the graph of Figure 19. The thicknesses were estimated by measuring the diameters of NWs before and after electrodeposition of CdSe. The variation of the CdSe thickness follows a linear evolution as a function of the applied charge density, confirming the pertinence of our results (Figure 19).

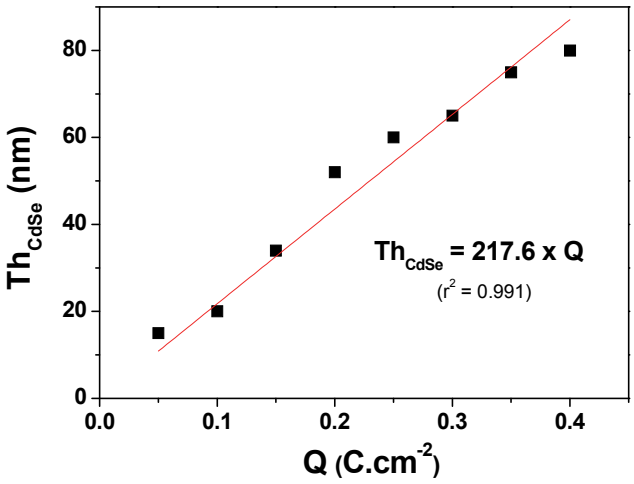


Figure 19 Estimated thickness of CdSe layers as a function of the applied charge density.

The absorbance of the TCO/ZnO_{ALD}/ZnO_{NWS}/CdSe samples has been determined from the reflectivity and transmission measurements (A=100-T-R). A quantification of these absorption spectra is made by calculating the effective absorption (A_E) in the region where CdSe absorbs (400-800 nm) and the results are displayed in the graph of Figure 20. We have determined the values of A_E from the following equation:

$$A_E = \int_{\lambda 1}^{\lambda 2} A(\lambda) J_0(\lambda) d\lambda \Big/ \int_{\lambda 1}^{\lambda 2} J_0(\lambda) d\lambda$$

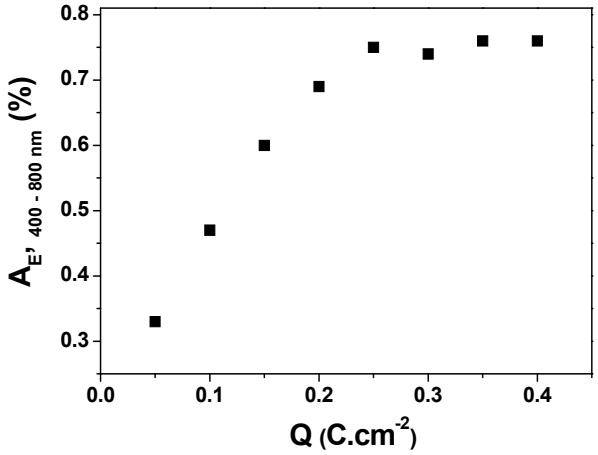


Figure 20 Effective absorbance of TCO/ZnO_{ALD}/ZnO_{NWS}/CdSe determined in this range 400-800 nm as a function of the applied charge density for CdSe deposition (i.e. CdSe thickness).

From the graph of Figure 20 we can clearly see that A_E was increased at least the double (from 33% to 75%) when the applied charge density is increased from 0.05 to 0.25 C.cm^{-2}, and reaches a plateau (~76%) after exceeding 0.25 C.cm^{-2}. This result is in accordance with the observation suggested from the SEM images of figure 18: higher than 0.25 C.cm^{-2} (thickness of ~ 60 nm of CdSe) the space between the NWs has been totally filled, resulting in the formation of a compact layer of CdSe. On the other hand, the effective absorbance for a 350 nm bulk layer of CdSe has been reported as equal to 56%.[30] This fact highlights the importance of the nanostructuration of the n-type semiconductor. In other terms, the light absorption enhances considerably (75%) by only coating our ordered urchin structures by as thin as 56 nm of CdSe layer.

Solar cells based on the core-shell ZnO-CdSe structures have been completed by infiltration of an equal amount of CuSCN (0.172 ml.cm^{-2}) leading to a thickness over the structures (ZnO/CdSe core-shell) of about ~2 µm. Finally a gold thin layer of about 100 nm was deposited on the previous deposited semiconductors in order to provide an electric contact for the ETA solar cell. The J-V characteristics of each cell have been measured under half sun (500 W/m^2) and the results are shown in Table 1.

Table 1 Characteristics of $ZnO_{Urchins}$/CdSe/CuSCN solar cells with different CdSe thickness

Q (C/cm^2)	Thickness $_{CdSe}$ (nm)	Jsc (mA/cm^2)	Voc (V)	FF
0.05	12	1.13	0.48	0.31
0.1	20	1.45	0.45	0.32
0.15	34	1.56	0.46	0.37
0.2	45	0.6	0.47	0.29
0.25	56	0.32	0.42	0.38
0.3	68	0.3	0.42	0.32
0.4	84	0.17	0.45	0.33

The variation of CdSe thickness from 12 to 84 nm has no noticeable influence on the open circuit voltage (V_{oc}) that remains mainly constant between 0.42 and 0.48 V. On the other hand, the values of the Short Circuit current density (J_{sc}) increase from 1.13 to 1.56 mA/cm^2 when the thickness increases from 12 to 34 nm, respectively. Thicker than 34 nm, the J_{sc} decreases gradually with the increase of the thickness. The photo-generated electron-hole pairs cannot be well separated which lead to a recombination increase, therefore, to a dramatic drop of the J_{sc}.

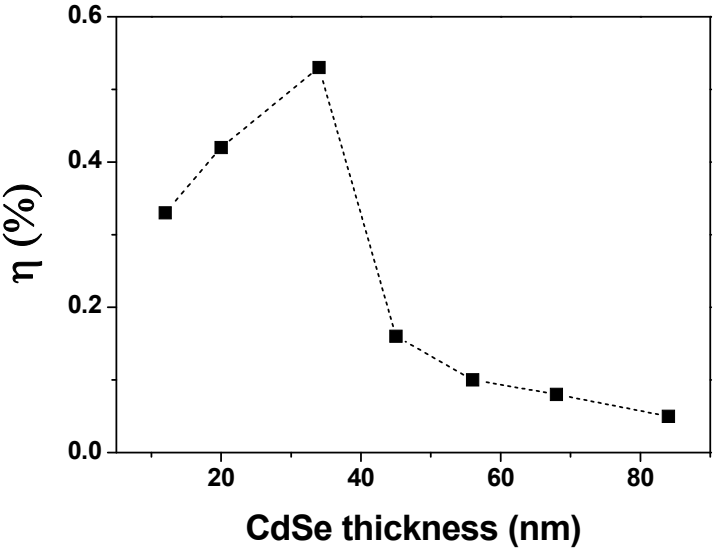


Figure 21 Conversion efficiency (η) as a function of CdSe thickness

As a partial conclusion for this study, the solar cell with about 30 nm CdSe thin layer gives rise to the optimal J_{sc} and allows an enhancement in the conversion efficiency up to 0.53% (Figure 21). Therefore, in the following studies the CdSe thickness will be fixed to about 30 nm.

6.3.2 Optimization of CuSCN thickness

Different thicknesses of CuSCN have been obtained by infiltrating different amount of saturated CuSCN solution. Volumes ranging from 102 to 242 µl.cm^{-2} were applied onto similar ZnO_{NW}/CdSe arrays (ZnO: L~0.45 µm, Φ ~113 nm, CdSe thickness ~30 nm). The solar cells have been completed by sputtering of a ~100 nm gold layer. The cross section SEM images of some CuSCN deposits are shown in Figure 22.

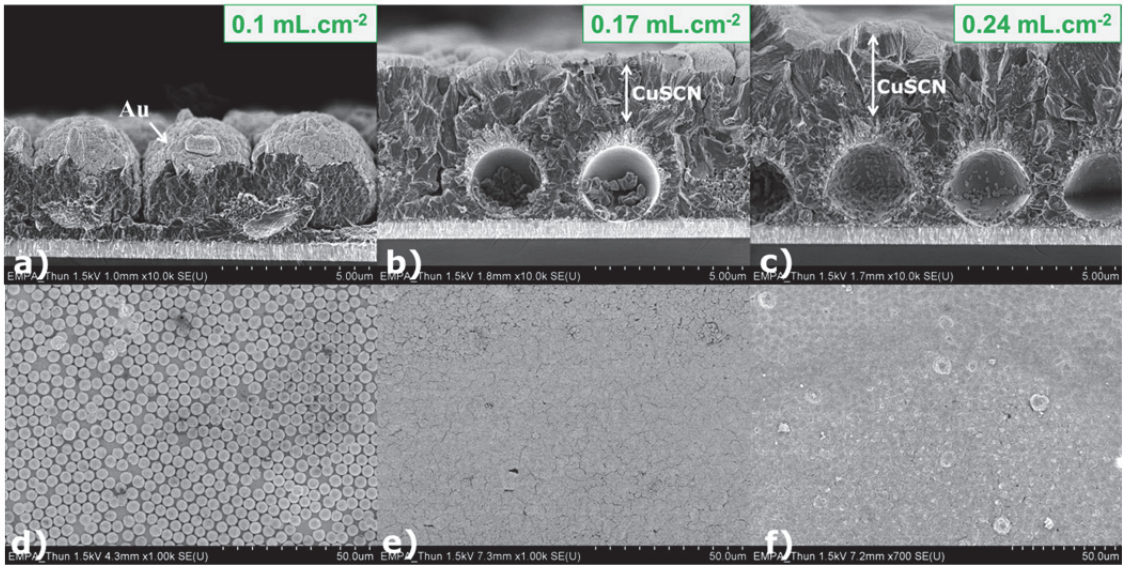


Figure 22 From a) to c): SEM Cross sections of ZnONWs/CdSe/CuCSN/Au solar cells with different thickness of CuSCN. d), e), and f): low magnifications SEM top view images of a), b) and c), respectively.

Figure 22a affirms that 0.1 mL.cm^{-2} is not enough to fill the interspace between the urchin-like nanostructures. A complete filling is obtained for volumes higher than 0.17 mL.cm^{-2} (Figures 22e and 22f). These solar cells exhibit flat surfaces required in order to obtain a good electrical contact avoiding short-circuit.

The above solar cell devices were completed by depositing a gold thin layer and the J-V curves were measured under half sun. As results, V_{oc} and the fill factor (FF) do not present significant evolution and remain in the range of 0.45 V and 34%, respectively. The differences obtained for the conversion efficiencies are mainly due to the variation of J_{sc}. The efficiency was increased from 0.23 to 0.53% when the CuSCN layer thickness increased from 0.68 to 1.85 µm above the nanostructured ZnO/CdSe urchins. The efficiency decreases when the thickness was higher than 1.85 µm. This optimal thickness is most probably related to the complete filling of the structure. The loss of current density and solar efficiency for the cells having thicknesses above 2.1 µm can be due to the increase of the electronic diffusion length which consequently leads to an increase in the carrier recombination. In the following parts of the project the CuSCN thickness was fixed to 1.85 µm above the urchin structures.

6.4 Role of nanostructuration on ETA performance

6.4.1 Light absorption

To study the effect of light scattering on the sensitization of the urchin-like building blocks we coated the series of different NW lengths shown in Figure 10 with a CdSe absorber film of constant thickness (~30 nm). Electrodeposited core-shell ZnO/CdSe structures with varying ZnO NW lengths from 300 to 1050 nm and a constant CdSe thickness of about 30 nm are shown in Figures 23a-d. Since the ZnO NW diameters were constant (~100 nm), a uniform ZnO/CdSe core-shell NW diameter (~160 nm) of these structures is seen in the high magnification images of Figure 23.

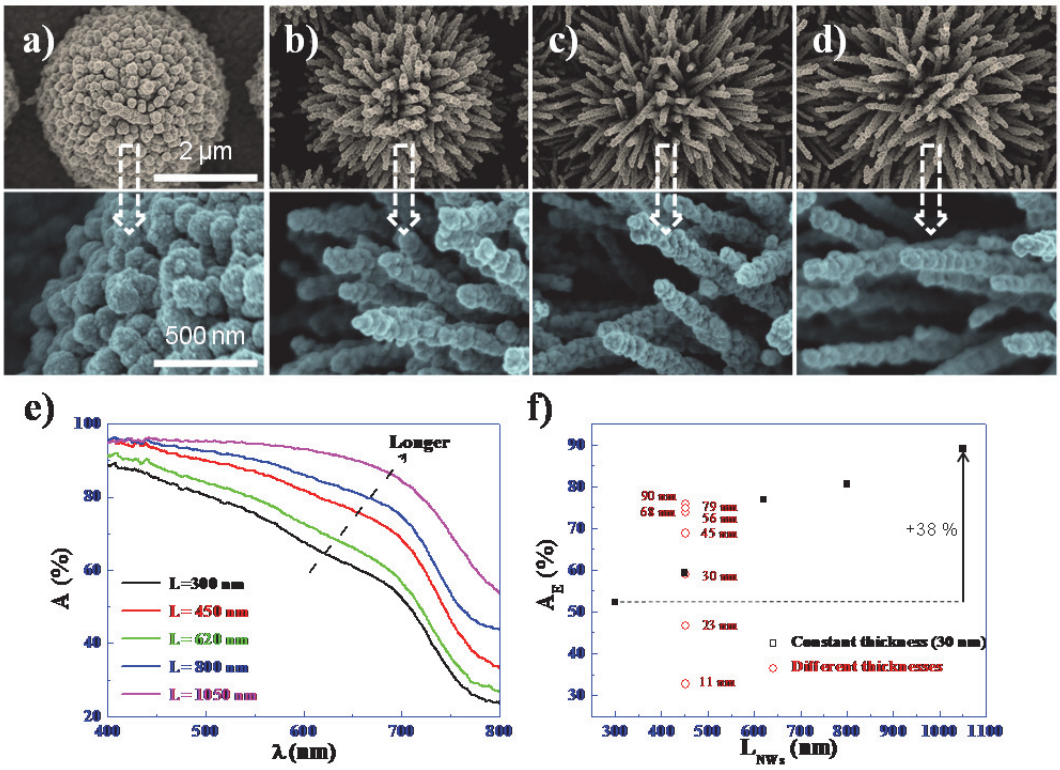


Figure 23 a-d) SEM images of conformal core-shell ZnO/CdSe urchin-like building blockswith varying lengths having constant CdSe thickness and ZnO NW diameter; e) The absorbance (A) spectra of the CdSe coated urchin building blocks; and f) Effective absorption (A_E) of ZnO/CdSe urchin-like building blocks versus ZnO NW length having a constant CdSe thickness of 30 nm. Also shown is the effective absorption for a constant NW length (450 nm) and varying CdSe thicknesses.

Figure 23e displays the absorbance (A) spectra resulting from measurements of the total transmittance and reflectance of the CdSe coated urchin-like building-blocks (A=100-T-R).

Compared to the reflectance graph of Figure 17b a clear correlation was detected for the absorbance after adding the CdSe layer, indicating that multiple scattering in the urchin-like structures enhances the optical absorption through ZnO/CdSe core-shell urchins. A quantification of these absorption spectra is made by calculating the effective absorption in the region where CdSe absorbs (400-800 nm) and the results are displayed in the graph of Figure 23f.

Figure 23f highlights the importance of the optical engineering of ZnO nanostructures on the light absorption. An increase of A_E from ~52% to ~90% is already obtained by increasing the NW lengths from 0.3 to 1µm (enhancement of 38%; dashed line in Figure 23f). In order to confirm the NW dimension effect on the scattering and the absorption, we fixed the length of NWs to ~450 nm and varied the thickness of CdSe absorber layer from 11 to 90 nm. The red circles in Figure 23e indicate that even by increasing the thickness up to 90 nm, the absorbance values were still lower than the one with the thinner CdSe layer (~30 nm) and longer NWs (~1 µm). This proves that the absorption of ZnO/CdSe core-shell building-blocks can be efficiently enhanced by our approach.

6.4.2 ETA performance

The final ZnO/CdSe/CuSCN ETA solar-cells were obtained by covering the core-shell ZnO/CdSe urchin-like building-blocks with CuSCN and a gold sputtered layer. A schematic view of the deposition process is shown in Figures 24a-c.

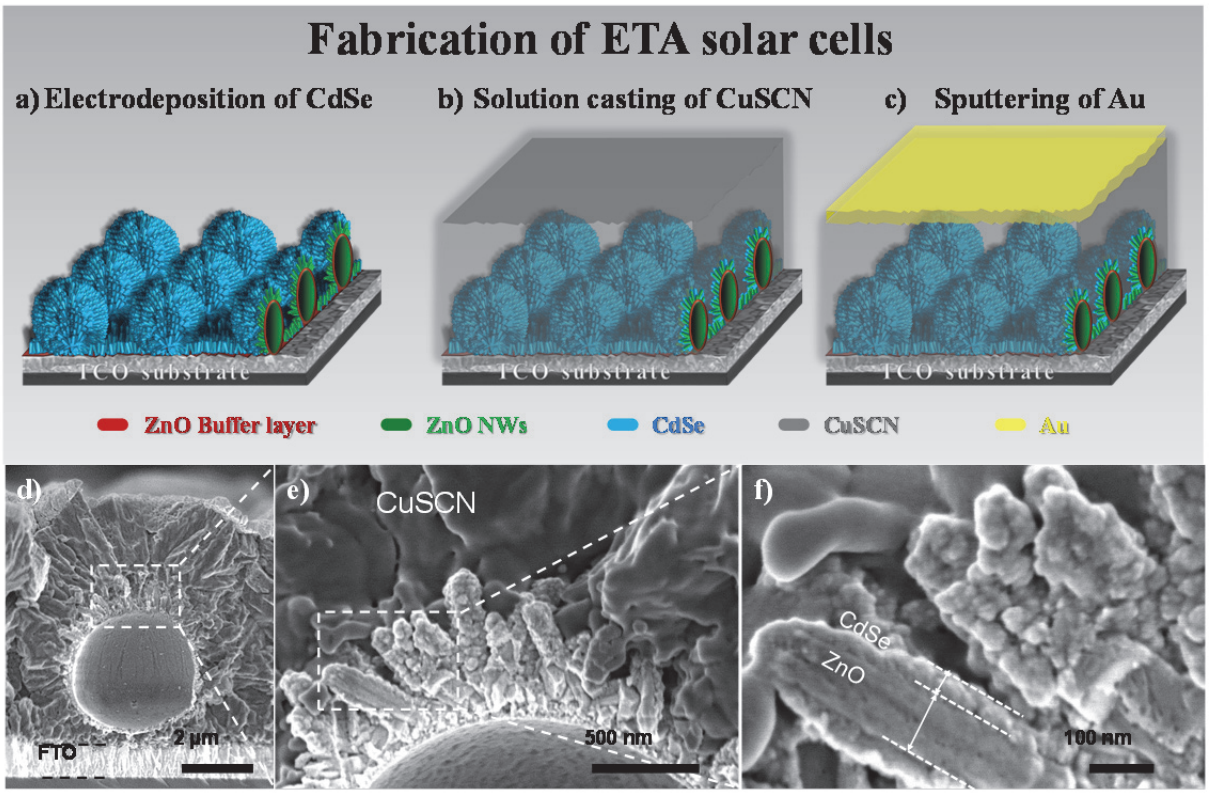


Figure 24 a-c) schematic view of the ETA solar cell. d-e) Cross-sectional SEM images of an individual urchin-like n-type ZnO building block (NWs: 100 nm diameter, 450 nm length) integrated in a fully processed solar-cell containing the CdSe absorber layer and p-type CuSCN.

Cross-sectional SEM images of a u-ZnO building-block in a fully processed solar-cell (diameter 100 nm, L_{NWs}~450 nm) are shown in Figures 24d-f. Figure 24d shows a high impregnation quality of CuSCN from the bottom to the top of the urchin nanostructure. The zooms taken at the interfaces of the ZnO/CdSe/CuSCN heterostructure (Figures 24e and 24f) confirm the good diffusion of the CuSCN solution and crystallization within the narrow interspace of NWs.

A mechanically scratched part of the core-shell ZnO/CdSe NW (dashed lines in Figure 24f) shows the high homogeneity of CdSe thickness (~30 nm) and the diameter of ZnO NW (~100 nm). Using a TEM cross-section lamella of another building block (L_{NW}~1 µm) for energy-dispersive X-ray mapping in a scanning transmission electron microscopy confirms that CdSe is homogeneously covering the urchin-like ZnO building-block as well as the NW carpet deposited directly on the FTO substrate (Figure 25). The same is true for the homogeneous infiltration by CuSCN.

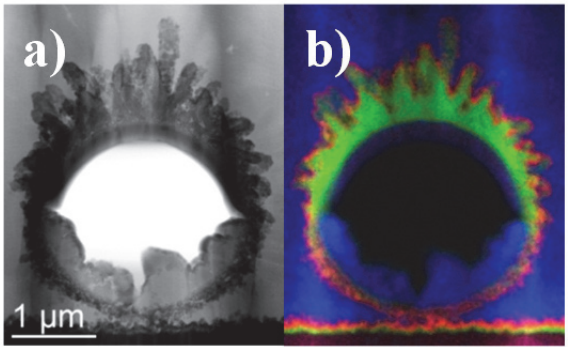


Figure 25 STEM image of an urchin building block (NWs: 100 nm diameter, length 1 µm) prepared as a 100 nm thin TEM lamella. The strong white contrast is due to the hollow nature of the building block.; e) EDX mapping made on (d), blue = Cu, purple = Cd, green = Zn, and black = vacuum. The presence of CuSCN inside the sphere is due to a preparation artefact.

Solar-cells based on urchin-like building-blocks with differing lengths of ZnO NWs were measured under 50 mW.cm^{-2} illumination conditions and the characteristics are displayed in Figure 26. It is clearly seen that J_{sc} values followed the same behaviour as A_E. The values of the open-circuit voltage (V_{oc}) and fill factor (FF) are almost constant with increasing NW length (Figure 26a).

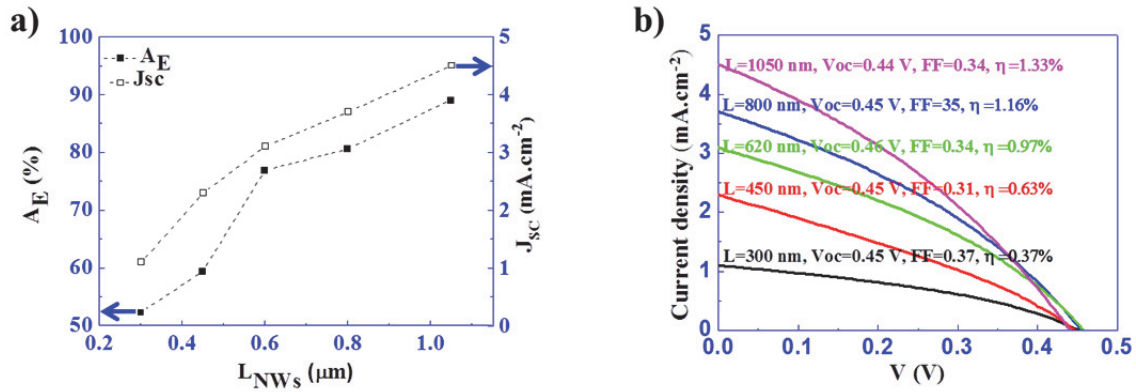


Figure 26 a) Short circuit current densities J_{sc} of solar-cells based on urchin-like building blocks having different lengths of ZnO NWs. For a direct comparison effective absorbance values (A_E) obtained in Figure 23d are displayed together; b) are the current density-voltage curves as a function of nanowire's length measured under half sun. All the solar characteristics are included in the graph.

The combination of these characteristics leads to an almost linear increase of the conversion efficiency (Figure 26a) from 0.37% to higher than 1.3% by only increasing the ZnO nanowire lengths from 300 to 1050 nm. These results prove, for the first time, that solar-cells can be made by three-dimensional, urchin-like ZnO nanowire building blocks. Although our actual best solar-cell efficiency is still slightly lower with respect to the few published works concerning ZnO/CdSe/CuSCN solar-cells (1.33% vs 2%), we strongly believe that there is a big potential for solar cell improvement by further optimizing the geometry of urchin-like ZnO nanowire building-blocks as well as for the optimization of absorber layer and hole collector layer thicknesses and materials.

7. Conclusions

In this project, we have established a novel low-cost synthesis route to produce large areas of perfectly-ordered hollow self-stabilized urchin-like ZnO nanowire building-blocks by a combination of polystyrene sphere patterning, atomic layer deposition, and electrodeposition. The process allows a wide control of the dimensions of arrays of urchin-inspired building building-blocks and their constituting ZnO nanowires. This method opens the door for investigations of a large class of semiconducting and metallic materials in more complex three-dimensional architectures for different type of applications, like short-wavelength lasers, piezoelectric nanogenerators, nanogenerators, electroluminescence, and field-emission devices. For the first time, we proved the functionality of this unique architecture in extremely thin absorber solar-cells. A clear correlation between the geometry of the urchin-like building block, the optical properties, and the solar efficiency has been stated offering promising applications of such building-blocks in different types of nanostructured solar-cells (organic, hybrid and dye sensitized solar-cells) as well as in applications where specific architectures of high surface area structures are an asset like for wettability, gas sensing, and biofuel cells. Although the actual efficiency still relatively low, many rooms of investigation are planned in the future research to improve the performance. First we believe that we had a full control in terms of control of the architecture of the n-type semiconductor (ZnO) and the optimal thickness of CdSe. In the following steps, the focus will be on the interfacial recombination and separation at the n-type|absorber interface. While spontaneous decay of charge carrier, recombination within the absorber may be efficiently suppressed due to the ETA-solar cell configuration; the substantially enlarged surface area is expected to lead to a considerable increase of interface recombination probability (as compared to a flat surface of the same optical density). Therefore, the aim is to add a shell passivation layer of transparent and wide band gap semiconductors (allowing light to reach the absorber) with low conductivity (through which electron tunneling can occur) on the core ZnO nanostructures in order to control/slow-down the active interface recombination kinetics. On the other hand, similar study will be performed at the absorber|p-type interface. In addition, we believe that the determination of the fundamental requirements for dopant incorporation into the p-type material will improve efficiently the performance of ETA solar cells. Ultimately, we hope to determine an optimal design of ETA solar cell enabling rise of conversion efficiency close to the predicted one.

8. Symbols used

Symbol	Unit	
A	%	Absorbance
A_E	%	Effective absorbance
FF		Fill factor
J_0	$W.cm^{-2}$	Photon flux
J_{SC}	$A.cm^{-2}$	Short-circuit current
L	nm or µm	Length of nanowire
Q	$C.cm^{-2}$	Charge density
R	%	Optical reflectance
T	%	Optical transmittance
Temp	°C	Temperature
Th_{CuSCN}	µm	Thickness of CuSCN over ZnO/CdSe arrays
V_{CuSCN}	$mL.cm^{-2}$	Volume of CuSCN saturated solution per coated surface area
V_{OC}	V	Open-circuit voltage

Φ	nm	Diameter of nanowires
□	%	Conversion efficiency
λ	nm	Wavelength
[]	$mol.L^{-1}$	Concentration of species

9. References

[1] B. Jalali, S. Fathpour, Silicon photonics, Journal of Lightwave Technology 24, 12, 4600-4615, 2006.
[2] J. Zhao, A. Wang, M.A. Green, 24.5% efficiency silicon PERT cells on MCZ substrates and 24.7% efficiency PERL cells on FZ substrates , Progress in Photovoltaics: Research and Applications, 7, 6, 471-474, 1999.
[3] Y. Liang, D. Feng, Y. Wu, S. Tsai, G. Li, C. Ray, L. Yu, Highly efficient solar cell polymers developed via fine-tuning of structural and electronic properties, Journal of the American Chemical Society 131 22, 7792-7799, 2009.
[4] B. O'Regan, M. Grätzel, Low-cost, high-efficiency solar cell based on dye-sensitized colloidal TiO_2 films, Nature 353 (6346), pp. 737-740, 1991.
[5] http://solarcellsinfo.com/dyecell/node/5713
[6] http://www.oled-display.net/organic-solar-cells-reach-6-confirmed-efficiency/
[7] Y. Li, J. Xiang, F. Qian, S. Gradečak, Y. Wu, H. Yan, D.A. Blom, C.M. Lieber, Dopant-free GaN/AlN/AlGaN radial nanowire heterostructures as high electron mobility transistors, Nano Letters, 6, 7, 1468-1473, 2006.
[8] X. Wang, J. Song, P. Li, J.H. Ryou, R.D. Dupuis, C.J. Summers, Z.L. Wang, Growth of uniformly aligned ZnO nanowire heterojunction arrays on GaN, AlN, and Al0.5Ga0.5N substrates, Journal of the American Chemical Society 127, 21, 7920-7923, 2005.
[9] Huang, M.H. et al. Room-temperature ultraviolet nanowire nanolasers. Science 292, 1897-1899 2001.
[10] Wang, Z.L. & Song, J.H. Piezoelectric nanogenerators based on zinc oxide nanowire arrays. Science 312, 242-246 2006.
[11] Park, W.I. & Yi, G.C. Electroluminescence in n-ZnO nanorod arrays vertically grown on p-GaN. Adv. Mater. 16, 87-+ 2004.
[12] Tseng, Y.K. et al. Characterization and field-emission properties of needle-like zinc oxide nanowires grown vertically on conductive zinc oxide films. Advanced Functional Materials 13, 811-814 2003.
[13] F.M. Ross, J. Tersoff, M. Reuter, Sawtooth faceting in silicon nanowires, Physical Review Letters 95 14, 146104, 1-4, 2005.
[14] S. Peulon, D. Lincot, Cathodic electrodeposition from aqueous solution of dense or open-structured zinc oxide films , Advanced Materials, 8, 2, 166-170, 1996.
[15] J. Elias, R. Tena-Zaera, C. Lévy-Clément, Electrochemical deposition of ZnO nanowire arrays with tailored dimensions, Journal of Electroanalytical Chemistry 621, 2, 171-177, 2008.
[16] C. Lévy-Clément, R. Tena-Zaera, M.A. Ryan, A. Katty, G. Hodes, CdSe-sensitized p-CuSCN/nanowire n-ZnO heterojunctions, Advanced Materials, 17, 12, 1512-1515, 2005
[17] R. Könenkamp, R.C. Word, C. Schlegel, Vertical nanowire light-emitting diode, Applied Physics Letters 85, 24, 6004-6006, 2004.
[18] Z.L. Wang, ZnO nanowire and nanobelt platform for nanotechnology , Materials Science and Engineering R: Reports 64, 3-4, 33-71, 2009.
[19] K. Taretto, U. Rau, J.H. Werner, Method to extract diffusion length from solar cell parameters - Application to polycrystalline silicon, Journal of Applied Physics 93, 5447-5455, 2003.
[20] S. Chu, D. Li, P.-C. Chang, J.G. Lu, Flexible Dye-Sensitized Solar Cell Based on Vertical ZnO Nanowire Arrays, Nanoscale Research Letters 6, 1-4, 2011.
[21] J.-S. Na, B. Gong, G. Scarel, G.N. Parsons, Surface polarity shielding and hierarchical ZnO nanoarchitectures produced using sequential hydrothermal crystal synthesis and thin film atomic layer deposition ACS Nano 3, 3191-3199, 2009-
[22] J. Elias, R. Tena-Zaera, C. Lévy-Clément, Effect of the chemical nature of the anions on the electrodeposition of ZnO nanowire arrays, Journal of Physical Chemistry C 112, 5736-5741, 2008.
[23] J. Elias, C. Lévy-Clément, M. Bechelany, J. Michler, G.-Y. Wang, Z. Wang, L. Philippe, Hollow urchin-like ZnO thin films by electrochemical deposition, Advanced Materials 22, 1607-1612, 2010.

[24] J. Elias, R. Tena-Zaera, C. Lévy-Clément, Electrodeposition of ZnO nanowires with controlled dimensions for photovoltaic applications: Role of buffer layer, Thin Solid Films 515, 8553-8557, 2007.
[25] J. Elias, R. Tena-Zaera, C. Lévy-Clément, Electrochemical deposition of ZnO nanowire arrays with tailored dimensions, Journal of Electroanalytical Chemistry 621, 171-177, 2008.
[26] R. Tena-Zaera, J. Elias, C. Lévy-Clément, ZnO nanowire arrays: Optical scattering and sensitization to solar light, Applied Physics Letters 93, art. no. 233119, 2008.
[27] R. Tena-Zaera, J. Elias, C. Lévy-Clément, Role of chloride ions on electrochemical deposition of ZnO nanowire arrays from O_2 reduction , Journal of Physical Chemistry C, 111, 16706-16711, 2007.
[28] V. Srikant, D.R. Clarke, On the optical band gap of zinc oxide , Journal of Applied Physics, 83, 5447-5451, 1998.
[29] C. F. Bohren and D. R. Huffman, Absorption and Scattering of Light by Small Particles Wiley, New York, Chap. 4, 1998.
[30] J. Elias, Ph.D. Réseaux de nanofils et de nanotubes d'oxyde de zinc de dimensions contrôlées obtenus par voie électrochimique : application aux cellules solaires nanostructurées, 1998.